SCIENTIFIC REPORTS

natureresearch

OPEN

Synthesis of $WS_{1.76}Te_{0.24}$ alloy through chemical vapor transport and its high-performance saturable absorption

Zhengting Du[1], Chi Zhang[1], Mudong Wang[2], Xuejin Zhang[1], Jian Ning[2], Xinjie Lv[1], Gang Zhao[1], Zhenda Xie[3]*, Jinlong Xu[3]* & Shining Zhu[1,2]

Layered transitional metal dichalcogenides (TMDs) are drawing significant attentions for the applications of optics and optoelectronics. To achieve optimal performances of functional devices, precisely controlled doping engineering of 2D TMDs alloys has provided a reasonable approach to tailor their physical and chemical properties. By the chemical vapor transport (CVT) method and liquid phase exfoliation technique, in this work, we synthesized $WS_{1.76}Te_{0.24}$ saturable absorber (SA) which exhibited high-performance of nonlinear optics. The nonlinear saturable absorption of the $WS_{1.76}Te_{0.24}$ SA was also measured by the open aperture Z-scan technique. Compared to that of the binary component WS_2 and WTe_2, $WS_{1.76}Te_{0.24}$ SA has shown 4 times deeper modulation depth, 28% lower saturable intensity and a much faster recovery time of 3.8 ps. The passively Q-switched laser based on $WS_{1.76}Te_{0.24}$ was more efficient, with pulse duration narrowed to 18%, threshold decreased to 28% and output power enlarged by 200%. The promising findings can provide a method to optimize performances of functional devices by doping engineering.

2D transitional metal dichalcogenides (TMDs) materials with formula MX_2 (M = Mo, W; X = S, Se, Te) have attracted intense attentions thanks to their unique layered structures, attractive carrier mobility, adjustable band-gap, strong light-matter interaction and stable chemical properties[1–9]. The abundant physical and chemical properties of TMDs are widely applied to photodetectors, logic devices, memories, catalysis, transistors and lasers. The discrepancy of strong covalent bonds intra layers and weak van der Waals inter layers allows down-top and top-down methods to obtain the 2D TMDs nanosheets. For example, chemical vapor deposition (CVD) and wet chemical synthesis are used to obtain the 2D TMDs nanosheets by the methods of down-top[10,11]. It is also desirable to combine two different mature methods of chemical vapor transport (CVT) and mechanical stripping to achieve the nanomaterials (top-down)[12,13]. TMDs can potentially serve as SAs, such as molybdenum disulfide and tungsten disulfide, which already exhibited promising applications with much larger modulation depth than graphene[14–18]. The band-gaps of MoS_2 and WS_2 are about 1.6~1.9 eV in the visible range, indicating the natural MoS_2 and WS_2 are far from serving as saturable absorbers in highly developed infrared lasers. In recent years, the defects have been introduced into TMDs in order to extend the bandwidth of TMDs SAs. It has been proved by theories and experiments that M or X vacancy defects in TMDs can reduce their band-gaps[19–22]. S. Wang reduced the band-gap of MoS_2 by introducing defects[19]. MoS_2 with S defects can be used as a broadband saturable absorber. The passively Q-switched lasers in the range of 1.06, 1.42 and 2.1 μm were realized based on the MoS_2 SA with S defects, corresponding pulse duration of 970, 729 and 410 ns, respectively[19]. X. Guan *et al.* experimentally realized 2.7 μm self-Q-switching laser of $Er:Y_2O_3$ based on WS_2 SA with pulse width of 1.36 μs[20]. The passively Q-switched lasers at the wavelengths of 1.5, 2.0, 2.7 μm are based on the binary TMDs with defects[14–22]. However, M or X vacancy defects in MX_2 make its structure unstable, so M or X vacancy defects in TMDs are difficult to repeatedly synthesized. Furthermore it is less feasible to regulate intentional defects, for example, the 2D MX_2 often appears to be both triangle and hexagon due to the local condition. Therefore, there is an urgent need to tune the band-gaps of the TMDs so that they can perform stably in the near-infrared and mid-infrared range.

[1]College of Engineering and Applied Sciences, Nanjing University, Nanjing, 210093, China. [2]School of Physics, Nanjing University, Nanjing, 210093, China. [3]School of Electronic Science and Engineering, Nanjing University, Nanjing, 210093, China. *email: xiezhenda@nju.edu.cn; longno.2@163.com

Inspired by the history of Si semiconductor, the doping engineering appears to be the key to tailor physical and chemical properties of TMDs. Mixed chalcogenides or mixed metal elements of two different TMDs can control the band gap, such as $WS_{2x}Se_{2(1-x)}$[23] and $Mo_xW_{1-x}S_2$[24]. However, it has been proven that only a few hundred milli-electron volts (meV) could be realized, i.e. 300 meV for $WS_{2x}Se_{2(1-x)}$ and 170 meV for $Mo_xW_{1-x}S_2$ solid solutions respectively. P. Yu *et al.* experimentally showed that 2H-WSe$_2$ and Td-WTe$_2$ can form stable layered $WSe_{2x}Te_{2(1-x)}$ alloys[25], with a phase transition from 2H-to-Td ($x = 1 - 0.6$ for 2 H structure; $x = 0.5$ and 0.4 for 2 H and 1 Td structures; $x = 0 - 0.3$ for 1 Td structure) controlled by the complete composition. The electronic structures changing from semiconducting to metallic enable wide tunability of the optical and electronic properties. Extraordinary physical properties of alloys are needed for in-depth study where the alloys showed some unique advantages compared to 2D binary TMDs, making them fundamentally and technically important in applications of optics and optoelectronics. One of the impressive physical properties of mono- and few-layer alloy is that TMDs display surprisingly excellent nonlinear optical properties, Y. Wang *et al.* studied the nonlinear optics properties of alloys of $Bi_2Te_xSe_{3-x}$ with lower saturable intensity, deeper modulation depth[26].

TMDs alloying still remains challenging resulted from the lattice mismatch of their parent counterparts. Here we synthesized $WS_{1.76}Te_{0.24}$ alloy by doping Te^{2-} ions in WS_2 (2 H) structure. The nonlinear optics properties of $WS_{1.76}Te_{0.24}$ SA were 4 times deeper modulation depth, 28% lower saturable intensity and a much faster recovery time of 3.8 ps compared to those of WS_2 and WTe_2. To find out whether pulsed laser's performance can be promoted by alloying, passively Q-switched lasers were investigated based on WS_2, $WS_{1.76}Te_{0.24}$ and WTe_2 SAs at the wavelength of 1060 nm. We found that the passively Q-switched laser based on $WS_{1.76}Te_{0.24}$ was more efficient, with pulse duration narrowed to 18%, threshold decreased to 28% and output power enlarged by 200%. The promising findings can provide a method to optimize performances of functional devices by doping engineering.

Methods

Synthesis and characterization of WS_xTe_{2-x} SAs.
The $WS_{1.76}Te_{0.24}$ monocrystalline was prepared by the chemical vapor transport (CVT) method with well-controlled temperature. There were two steps to obtain $WS_{1.76}Te_{0.24}$ mono-crystalline. Firstly, $WS_{1.76}Te_{0.24}$ polycrystalline was synthesized by heating a mixture of sulphur (Strem Chemicals 99.9%), tungsten (Strem Chemicals 99.9%) and tellurium (Strem Chemicals 99.9%) with stoichiometric amounts at 750 °C for 48 hours in an evacuated and sealed quartz ampoule (8 mm ID, 10 mm OD, 300 mm length). Considering the powerful exothermicity of the reaction, the mixture was slowly preheated to 750 °C for 12 hours to avoid explosion. Secondly, $WS_{1.76}Te_{0.24}$ was grown by CVT method in a double zone furnace with as-prepared grinded polycrystalline powder and the transport agent was bromine (Sigma-Aldrich, 99.8%) at about 5 mg/mL. The procedure of growth was 72 hours in an evacuated and sealed quartz ampoule (8 mm ID, 10 mm OD, 300 mm length). Figure 1a showed a two-temperature zone tube furnace with well-controlled temperature. Throughout the growth process of $WS_{1.76}Te_{0.24}$, the raw material (T_2) and crystal growth zones (T_1) were kept at 1030 °C and 1010 °C, respectively. The parent components of WS_2 and WTe_2 were synthesized by the same method for the following contrast experiments. Figure 1b–d show the monocrystalline photographs and atomic structures of $WS_{1.76}Te_{0.24}$, WS_2 and WTe_2.

We prepared WS_2, $WS_{1.76}Te_{0.24}$ and WTe_2 SAs by liquid-phase exfoliation and spin-coating technique with the same parameters (sonication time, speed of centrifugation and spin-coating) for further comparison. First, the mixture of grinded 0.2 mg $WS_{1.76}Te_{0.24}$ monocrystalline in 4 ml acetone solvent was sonicated in high power for 40 min. Only pure acetone was employed as the solvent to avoid introduction of extra impurities. Then, we collected the one-third top of the dispersions after the centrifugation at 2500 rpm for 10 min to remove the large sedimentations. Finally, we span and coated the dispersion on SiO_2 plate to obtain $WS_{1.76}Te_{0.24}$ SA after the acetone was easily removed by volatilization in the air.

Material characterization.
Transmission electron microscopy (TEM) and energy dispersive spectroscopy (EDS) were adopted to learn the morphology of the $WS_{1.76}Te_{0.24}$ nanoplates. TEM images in Fig. 1e–g showed the layered structures of WS_2, $WS_{1.76}Te_{0.24}$ and WTe_2 respectively, where the gray scale was directly proportional to the thickness. The observed well exfoliated nanoflakes with layered structure implied rigid mechanical property. The insets were the Selected Area Electron Diffraction (SAED) of WS_2, $WS_{1.76}Te_{0.24}$ and WTe_2 nanoflakes. The SAED showed that WS_2, $WS_{1.76}Te_{0.24}$ and WTe_2 were monocrystalline with 2 H, 2 H and Td phases, respectively. The diffraction of six-fold symmetry spots displayed the hexagonal lattice of $WS_{1.76}Te_{0.24}$ nanoflake. EDS measurement was also produced to determinate the element ratio of the three samples as shown in Fig. 1h–j. It can be seen that the ratio of S to Te in $WS_{1.76}Te_{0.24}$ is 1.76 to 0.24, indicating an efficient doping of Te ions in WS_2 framework. As shown in Fig. 1k–m, the atomic force microscopy (AFM) was carried out to measure the three SAs thicknesses. The thicknesses of WS_2, $WS_{1.76}Te_{0.24}$ and WTe_2 nanoflakes were about 15.6, 14.9, and 16.3 nm, corresponding to 23, 19 and 27 layers, respectively. To learn more about the $WS_{1.76}Te_{0.24}$ alloy, EDS mapping was adopted shown in Fig. 1n. The green, red and yellow parts were the distribution of tungsten, sulphur, and tellurium element, respectively. The uniform doping of Te in WS_2 of $WS_{1.76}Te_{0.24}$ was obtained. Furthermore, the $WS_{1.76}Te_{0.24}$ SA with no additional dangling bonds is stable in the air. The high chemical stability was due to the substitution of atoms in the alloy TMDs.

Raman spectroscopy was employed to learn the detailed lattice vibration modes of $WS_{1.76}Te_{0.24}$ affected by doping engineering where Te^{2-} replaced the S^{2-} in the WS_2 structure. The characterization was carried out by using a Jobin Yvon LabRam 1B Raman spectrometer with laser source at 532 nm. The comparison of the Raman fingerprints among the three samples in the range of 200–450 cm^{-1} is shown in Fig. 2a. In Fig. 2a, the characteristic peaks at 353.2 and 422.7 cm^{-1} were assigned as the in-plane (E_{2g}) and out-of-plane (A_{1g}) vibrational modes corresponding to WS_2 nanoflakes. For the Td-WTe$_2$, the spectrum just showed the A_1 Raman mode at 217.8 cm^{-1}. The characteristic bands of $WS_{1.76}Te_{0.24}$ showed the "two mode behavior" as the coexistence of vibrations of WS_2
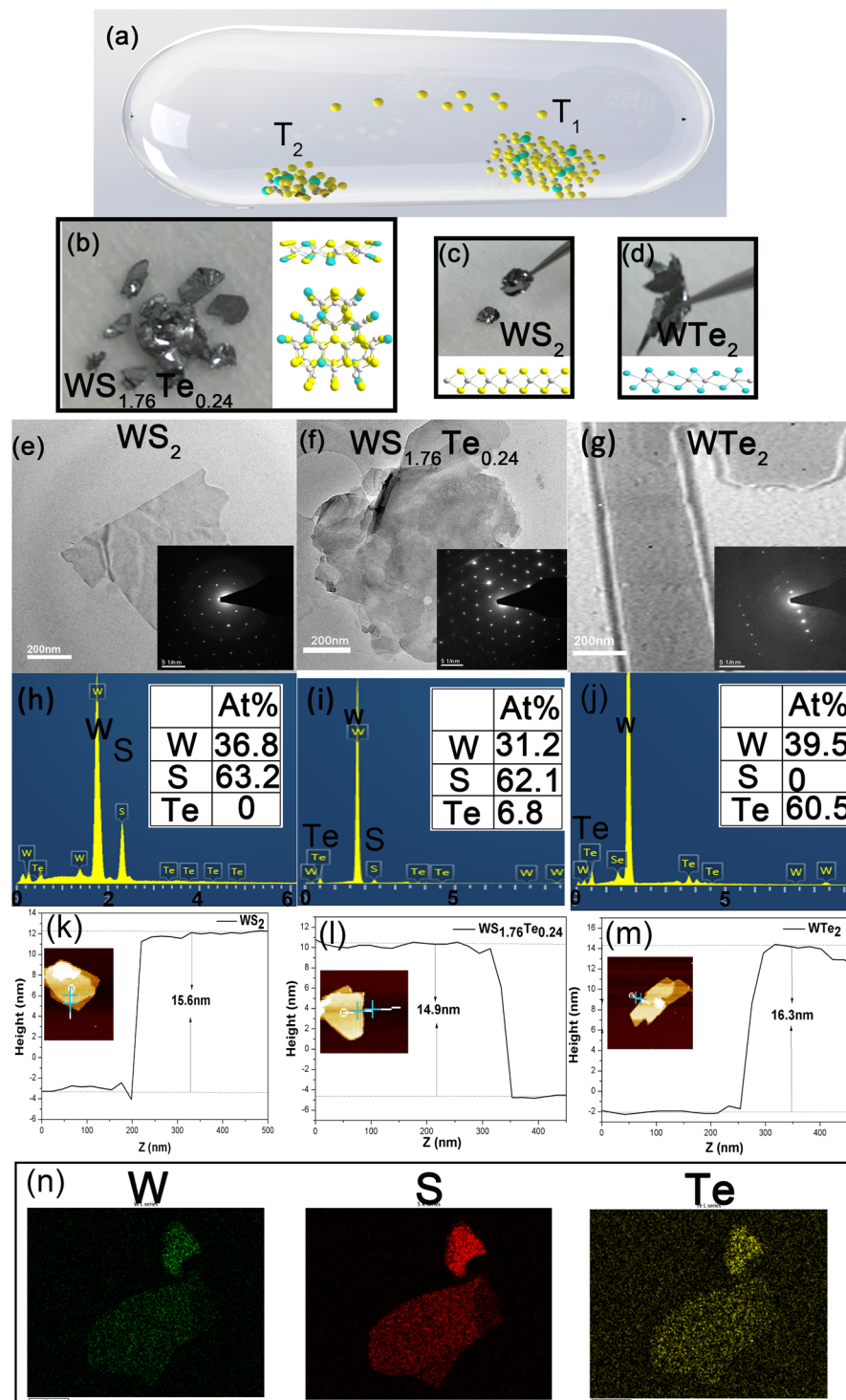
Figure 1. (**a**) Scheme of chemical vapor transport (CVT) for crystallization of WS_xTe_{2-x} in a temperature gradient. Monocrystalline photograph and atomic structure of (**b**) $WS_{1.76}Te_{0.24}$. (**c**) WS_2. (**d**) WTe_2. TEM and SEAD characterizations of few-layer nanosheets of (**e**) WS_2, (**f**) $WS_{1.76}Te_{0.24}$ and (**g**) WTe_2. Corresponding full EDS scanning of (**h**) WS_2, (**i**) $WS_{1.76}Te_{0.24}$ and (**j**) WTe_2. AFM images and thickness measurement of typical nanosheets and height measurement recorded at different sections of (**k**) WS_2, (**l**) $WS_{1.76}Te_{0.24}$ and (**m**) WTe_2. (**n**) EDS mapping of $WS_{1.76}Te_{0.24}$. The clear morphology implies the uniformity of component distribution.

and WTe_2. The E_{2g} and A_{1g} peaks of $WS_{1.76}Te_{0.24}$ at 352.5 and 411.5 cm^{-1} are resulted from the corresponding modes in WS_2. The red-shift of A_{1g} (0.7 cm^{-1}) and E_{2g} (11.2 cm^{-1}) mode is attributed to the significant changes in the electron-phonon coupling soften by the doping of Te. The frequency broadened at A_1 (217.8 cm^{-1}) was
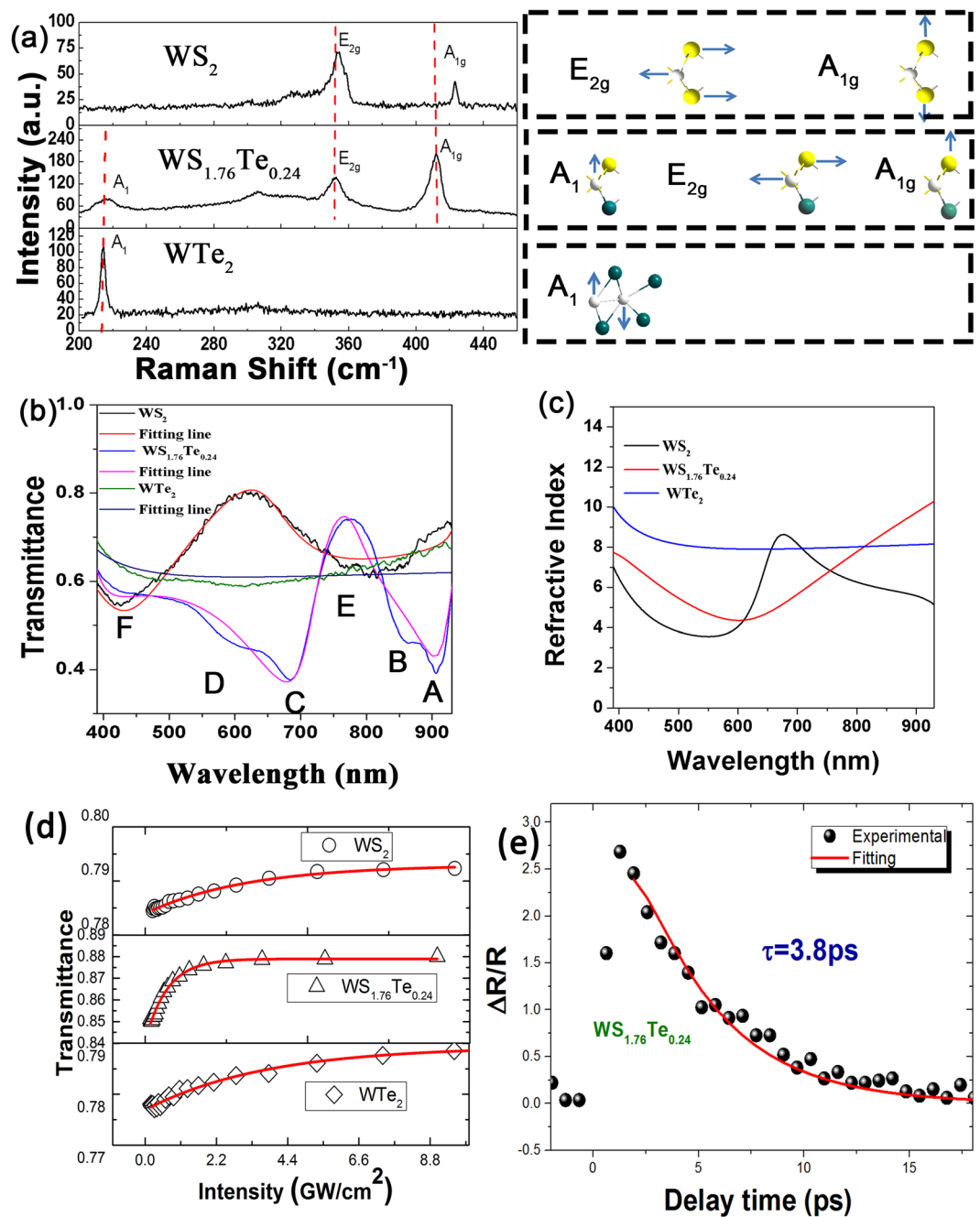
Figure 2. (a) Raman spectra and vibration modes of few-layer $WS_{1.76}Te_{0.24}$ nanosheets. (b) Comparison of recorded transmittance spectra and corresponding fitted line of WS_2, $WS_{1.76}Te_{0.24}$ and WTe_2. (c) The refractive index of WS_2, $WS_{1.76}Te_{0.24}$ and WTe_2 based on the relationship of Kramers-Kronig. (d)The open-aperture Z-scan measurements of WS_2, $WS_{1.76}Te_{0.24}$ and WTe_2 flakes at 1060 nm. (e) An ultrafast signal of $WS_{1.76}Te_{0.24}$ proved that the relaxation time was ~3.8 ps.

originated from the reduced structural symmetry arising from lattice distortion due to the different atomic radius of Te and S. In earlier studies, TMDs alloys, e.g. $Mo_xW_{1-x}S_2$[24] and $WS_{2x}Se_{2(1-x)}$[23], have the similar frequency shift. The Raman shifts further confirm the expected structural and compositional evolution in the $WS_{1.76}Te_{0.24}$ alloy.

Figure 2b showed linear transmittance spectra of $WS_{1.76}Te_{0.24}$ SA with WS_2 and WTe_2 as contrasts. The typical absorption peaks of $WS_{1.76}Te_{0.24}$ corresponded to the trait of TMD 2 H phase. The peaks located at the wavelength of 906 (A) and 859 nm (B) coincided with inter-band transitions. A, B are resulted from spin-orbit splitting of transitions[16], while C and D (685 and 592 nm) are due to the higher density transition[16]. The transmittance spectrum of WS_2 showed the TMD absorption with absorption peaks at 814 (E) and 426 (F) nm. WTe_2 displayed semi-metallic phase absorption characteristic with broadband absorption. According to the Tauc plot by extrapolating the linear absorption versus photon energy curve, optical bandgaps of $WS_{1.76}Te_{0.24}$, WS_2 SAs were calculated

Materials	n	α_0 (10^4 cm^{-1})	α_{NL} (10^4 cm/GW)	Im$\chi^{(3)}$ (10^{-7} esu)	FOM (10^{-14} cm•esu)	As (%)	I_S (GW/cm^2)
WS$_2$	6.19	0.90	−0.41	−4.98	5.53	1.15	3.15
WS$_{1.76}$Te$_{0.24}$	10.2	2.25	−0.53	−17.5	7.78	4.47	0.89
WTe$_2$	8.29	1.08	−0.38	−8.28	7.66	1.60	3.70

Table 1. SA Results for Different Two-dimensional Materials.
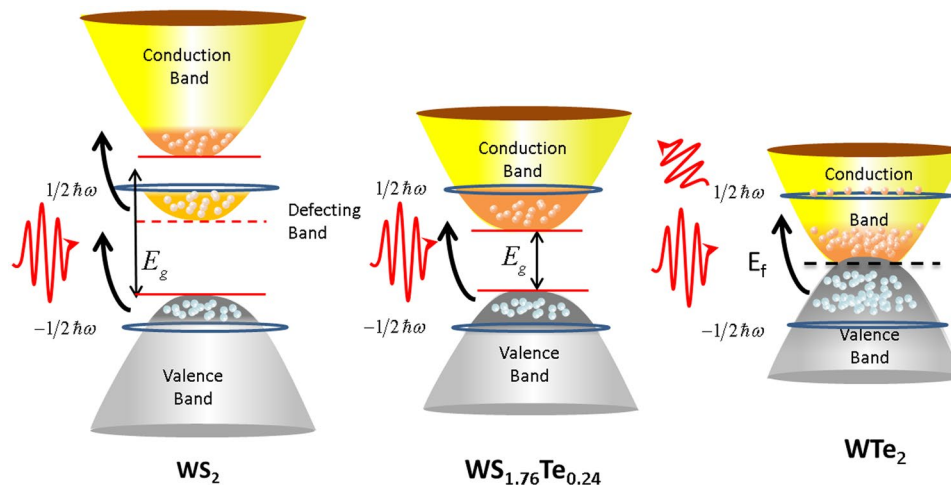

Figure 3. Schematic diagram of linear absorption in WS$_2$, WS$_{1.76}$Te$_{0.24}$ and WTe$_2$ SAs.

to be 1.2 eV and 1.9 eV, respectively. The electronic structure of WS$_{1.76}$Te$_{0.24}$ strongly depends on the coordination environment of W and its d-electron counts. The Te doping in WS$_2$ shorten band gap by the change coordination environment of W corresponding to the *ab initio*[23]. Thus physics properties of WS$_{1.76}$Te$_{0.24}$ were tailored by ion doping.

The ellipsometer is a conventional method to measure the film's refractive index. However, ellipsometer has strict requirement on the samples for uniform surface, large size, and thin thickness. Due to its low spatial resolution, it is difficult to obtain refractive index of nanomaterials in nanometer size. Benefitting from the Lorentz-Drude model and Kramers-Kronig (K-K) relationship of the dielectric function[27], we calculated the corresponding refractive index from the transmittance spectrum. Figure 2c shows the fitting curve of the reflectance spectra, where the refractive index parameters were obtained by the K-K relationship.

In order to understand the incorporation mechanism by Te doping into WS$_2$ and the corresponding effect on optical nonlinear properties of 2D WS$_{1.76}$Te$_{0.24}$, we performed Z-scan measurement with a femtosecond laser (1060 nm, 175 fs) as excited source. The results of WS$_2$, WS$_{1.76}$Te$_{0.24}$ and WTe$_2$ SAs are showed in Fig. 2d. The increase of transmittance was easily observed with the increase of laser intensity, resulted from the nonlinear saturable absorption effect. The mechanism of saturable absorption can be explained as Pauli blocking principle in the conduction band. However, significant differences in saturable absorption efficiency and sensitivity among the three samples can be clearly distinguished in Fig. 2d. Based on the nonlinear optical theory, the transmittance is expressed in the form of[14]

$$\mathrm{T} = 1 - A_s \cdot \exp\left(-\frac{I}{I_{sat}}\right) - A_{ns}$$

(1)

where A_s is the modulation depth, A_{ns} is the non-saturable components, I_{sat} is the saturable intensity, and I is the incident light intensity. The data was fitted with the Eq. 1, the modulation depth and the saturable intensities were obtained as presented in Table 1. The WS$_{1.76}$Te$_{0.24}$ saturation intensity and modulation depth were 0.88 GW/cm^2 and 4.47% respectively. When WS$_2$ became saturated above threshold of 3.15 GW/cm^2, the modulation depth was 1.14%. The saturation intensity and modulation depth of WTe$_2$ were 3.7 GW/cm^2 and 1.6%, respectively. Compared to binary component of WS$_2$ and WTe$_2$ SA, WS$_{1.76}$Te$_{0.24}$ SA performed 4 times deeper modulation depth and 28% lower saturable intensity, resulting from bandgap evolution of WS$_{1.76}$Te$_{0.24}$.

The bandgap evolution of WS$_{1.76}$Te$_{0.24}$ is used to interpret the lower saturable intensity. As shown in the Fig. 3, the bandgap of WS$_2$ SA is 1.9 eV larger than the photon energy ($\hbar\omega$) of 1060 nm laser. The saturable absorption of WS$_2$ is resulted from the defect states. As shown in Fig. 3, under the excited light, the electrons in valence band of WS$_2$ are transferred to the defect states. The electrons in the defect states jump to the conduction band with one more photon each. Therefore, there are two platforms that the transition of one electron from valence band to conduction band of WS$_2$ and the transition requires two photons. Compared to that of WS$_2$, the optical bandgap

of $WS_{1.76}Te_{0.24}$ is 1.2 eV covering 1.0 μm, so the electrons directly transfer from valence band to the conduction band with one absorbed photon. In WTe_2, the semi-metal characteristic makes it possess higher electron concentration in the conduction band. The higher concentration of electrons has stronger reflection on the excitation light as shown in Fig. 3. Therefore, compared to the binary component of WS_2 and WTe_2, $WS_{1.76}Te_{0.24}$ has stronger photon absorption at 1.0 μm. The stronger photon absorption of $WS_{1.76}Te_{0.24}$ can increase the number of absorbed photons to produce more electrons at the same laser intensity. Eventually, the saturable intensity of $WS_{1.76}Te_{0.24}$ is lowered.

Suppose at a certain photon frequency, optical absorption satisfies $\frac{dI}{dz'} = -\alpha(I)I$. Here the absorption coefficient $\alpha(I)$ is expressed as $\alpha(I) = \alpha_0 + \alpha_{NL}I$. dz' is the propagation distance in the sample. The third-order nonlinear optics susceptibility $Im\chi^{(3)}$ can be expressed as

$$Im\chi^3(esu) = (10^{-7}c\lambda n^2/96\pi^2)\alpha_{NL} \ (cm/W) \tag{2}$$

here c is the speed of light, λ is the laser wavelength, n is the refractive index, the discrepancy caused by the linear absorption, namely figure of merit (FOM): $FOM = |Im\chi^{(3)}/\alpha_0|$. Based on the model 2, we can obtain $WS_{1.76}Te_{0.24}$ with $\alpha_{NL} \sim -10^4$ cm/GW, $Im\chi^{(3)} \sim 10^{-7}$ esu, FOM $\sim 10^{-14}$ cm• esu. Compared to previous works, the FOM of $WS_{1.76}Te_{0.24}$ perform one order of magnitude larger than that of grapheme, graphene oxide, MoS_2/NMP dispersions $\sim 10^{-15}$ esu cm[16]. That suggests a promising potential to achieve efficient nonlinear performance by alloying TMDs. However, one should note that FOM varies with the different experiment conditions such as the wavelength, pulse width and so on. For convincing comparison, we carried out the Z-scan on the same condition and the nanosheets were prepared by the same parameters of liquid-phase exfoliation and spin-coating technique. The results are shown in Table 1. It is unambiguous that the FOM value of $WS_{1.76}Te_{0.24}$ SA was larger than those of WS_2 and WTe_2 SAs, which indicated the enhanced nonlinear performance of $WS_{1.76}Te_{0.24}$.

The pump-probe system was adopted to study the carrier relaxation that reflects the optical response of materials. The undegenerated pump probe system is easy to align and the relaxation time is corresponded to the carrier-phonon coupling[28]. The ultrafast signal was measured using a Ti: Sapphire laser with pulse duration of 120 fs, repetition rate of 76 MHz, fluence of 200 μJ/cm^2 at 395 nm as the pump and the probe beam was at 790 nm with much lower fluence. The probe reflection was a function of the delay time that was detected by a Si photodetector and amplified by a lock-in amplifier. As shown in Fig. 2e, the ultrafast signal of $WS_{1.76}Te_{0.24}$ flakes with absorption bleaching was obtained. The signal amplitude was as large as ~ 250%, implying excellent nonlinear optics property. Notably, the decay time was 3.8 ps fitted by a single exponential function. The decay time of $WS_{1.76}Te_{0.24}$ was significantly shorter than 13 ps of WS_2[29] and 5 ps of WTe_2[6], as a result of higher density of trapping states induced by Te doping in the nanoflake[30].

Investigation of the $WS_{1.76}Te_{0.24}$ saturable absorption in passively Q switched laser at 1.0 μm.
To identify whether the boosted saturable absorption effect of $WS_{1.76}Te_{0.24}$ did favor in Q-switched laser, we set up a passively Q-switched Yb: $Gd_2SrAl_2O_7$ (Yb: GSAO) laser to investigate the performance of WS_2, $WS_{1.76}Te_{0.24}$ and WTe_2 SAs. In Fig. 4a, the schematic of experiment setup was shown. A laser diode of 976 nm was served as pump source, which was coupled in a fiber of a core diameter of 105μm and the numerical aperture of 0.22. A doublet lens was employed to focus the beam at 105 μm within the Yb:GSAO crystal. In a cooled down system, the Yb: GSAO gain medium was wrapped with indium foil and mounted in a copper holder with water-cooled at 21 °C. The 11 mm linear cavity composed of 1060 nm high reflectivity M1(R = −200 mm) and 18% transmittance plano M2. The as-prepared three samples on SiO_2 were inserted into the cavity serving as the saturable absorber.

Figure 4b–d show the characteristics of average output power, repetition rates and pulse durations of the lasers on absorbed pump power variation. The absorbed pump power thresholds of WS_2, WTe_2, and $WS_{1.76}Te_{0.24}$ were 1.02, 1.21 and 0.34 W, respectively. The threshold of the $WS_{1.76}Te_{0.24}$ SA decreased to 28% due to the lower saturable intensity, as shown in Table 1. The output power was measured and calculated to be linearly correlated with the pump power. The maximum output powers of WS_2, WTe_2 and $WS_{1.76}Te_{0.24}$ were 247.5, 152.8 and 350 mW, respectively. It is worth noting that $WS_{1.76}Te_{0.24}$ SA achieved twice larger output power of WTe_2. The repetition rate continuously increased from 108.2 to 195.2 kHz for WS_2 SA, and the repetition rate range of $WS_{1.76}Te_{0.24}$ SA was 120.8 to 271.1 kHz, scope of WTe_2 varied from 112.2 to 170.8 kHz. As shown in Fig. 4d–f, pulse widths of 1.285 μs, 230 ns and 550 ns were obtained in 1.06 μm Q-switched lasers based on WS_2, $WS_{1.76}Te_{0.24}$ and WTe_2 SAs, respectively. As shown in Fig. 4e, the typical Q-switched pulse trains of WS_2, $WS_{1.76}Te_{0.24}$ and WTe_2 were recorded by a 500 MHz bandwidth oscilloscope (Tektronix, DPO7054) through a high-speed detector (Thorlabs, DET10C/M), which confirms the stability of Q-switched operation. The narrowest pulse duration was obtained by $WS_{1.76}Te_{0.24}$ SA that should be attributed to the much larger modulation depth than WS_2 and WTe_2 (Fig. 2d and Table 1). The passively Q-switched laser based on $WS_{1.76}Te_{0.24}$ narrowed pulse duration to 18%. The optical spectra of the Q-switched lasers were measured with an infrared optical spectrum analyzer (Yokogawa, AQ-6315A) with a resolution of 0.05 nm. The wavelength of WS_2, $WS_{1.76}Te_{0.24}$ and WTe_2 were centered at 1061.13 nm with 0.12 nm full width at half maximum (FWHM), 1065.93 nm with 0.45 nm FWHM, and 1058.01 nm with 0.16 nm FWHM, respectively. Q-switched laser based on the $WS_{1.76}Te_{0.24}$ SA can improve the key parameters as pulse width, slope efficiency and the average output power as listed in Table 2.

Conclusion
In this work, we have experimentally demonstrated the enhanced nonlinear optical properties of $WS_{1.76}Te_{0.24}$ by alloying WTe_2 and WS_2. We synthesized ternary $WS_{1.76}Te_{0.24}$ by CVT method. The SAED, EDS and Raman spectra showed good quality of the alloy $WS_{1.76}Te_{0.24}$ nanosheets. The saturable absorption of $WS_{1.76}Te_{0.24}$ at 1.06 μm was significantly more efficient than binary parents WTe_2 and WS_2 as evidenced by Z-scan and pump-probe results,
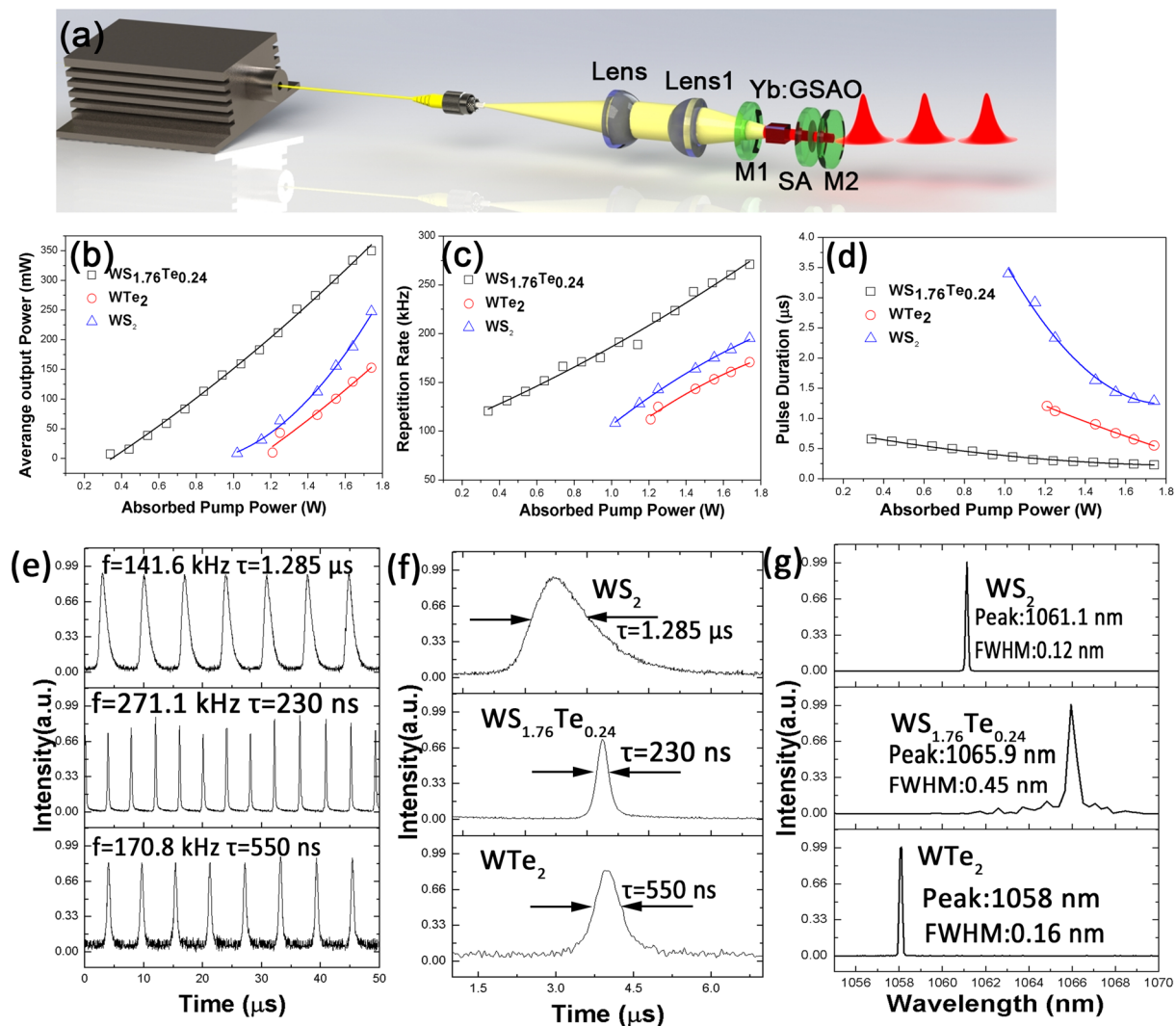
Figure 4. (**a**) Experimental setup of the LD pumped passively Q-switched Yb: GSAO laser at 1060 nm. (**b**)The output powers with increasing incident pump powers. (**c**) Pulse repetition rates. (**d**) Variations of pulse duration with increasing pump powers. The Q-switched lasers performance by the WS_2, $WS_{1.76}Te_{0.24}$ and WTe_2 SAs: (**e**) the oscilloscope tracings. (**f**) the single pulse tracings (**g**) the optical spectra.

Sample	WS_2	$WS_{1.76}Te_{0.24}$	WTe_2
Wavelength (nm)	1061.1	1065.9	1058.0
Output power (mW)	247.5	350	152.8
Pulse Duration	1.285 µs	230 ns	550 ns
Repetition rate (kHz)	141.6	271.1	170.8

Table 2. Experiment results of Q-switched lasers based on three SAs.

where $WS_{1.76}Te_{0.24}$ SA showed 4 times deeper modulation depth, 28% lower saturable intensity and a much faster recovery time of 3.8 ps. The passively Q-switched laser based on $WS_{1.76}Te_{0.24}$ was found more efficient, with pulse duration narrowed to 18%, threshold decreased to 28% and output power enlarged twice. The doping engineering SAs can improve the Q-switched lasers performance with lower energy consumption, narrower pulse width, and larger average output power. The promising findings can provide a method to optimize performances of functional devices by doping engineering.

Data availability

Data Availability For original data, please contact xiezhenda@nju.edu.cn.

References

1. Zhu, X. *et al*. TiS_2-based saturable absorber for ultrafast fiber lasers. *Photonics Research.* **6**, 50–54 (2018).
2. Liu, J., Raja, A. S., Karpov, M., Ghadiani, B. & Kippenberg, T. J. Ultralow-power chip-based soliton microcombs for photonic integration. *Optica.* **5**, 1347 (2018).
3. Wang, X. *et al*. Chemical vapor deposition growth of crystalline monolayer MoSe2. *Acs Nano.* **8**, 5125–5131 (2014).
4. Apte, A. *et al*. Structural Phase Transformation in Strained Monolayer MoWSe2 Alloy. *Acs Nano.* **12**, 3468–3476 (2018).
5. Zhu, Y. Q., Hsu, W. K., Kroto, H. W. & Walton, D. R. Carbon nanotube template promoted growth of NbS2 nanotubes/nanorods. *Chemical Communications.* **2001**, 2184 (2001).
6. Dai, Y. M. *et al*. Ultrafast Carrier Dynamics in the Large Magnetoresistance Material WTe2. *Phys.Rev.b.* **92**, 161104(R) (2015).
7. Cho, S. Phase patterning for ohmic homojunction contact in MoTe 2. *Science.* **349**, 625–628 (2015).
8. Zheng, F. *et al*. On the Quantum Spin Hall Gap of Monolayer 1T'-WTe2. *Advanced Materials.* **28**, 4845–4851 (2016).
9. Hao, L. *et al*. Femtosecond pulse erbium-doped fiber laser by a few-layer MoS(2) saturable absorber. *Optics Letters.* **39**, 4591-4594 (2014).
10. Keng-Ku, L. Growth of large-area and highly crystalline MoS2 thin layers on insulating substrates. *Nano letters.* **3** (2012).
11. Shi, Y. *et al*. van der Waals Epitaxy of MoS2 Layers Using Graphene As Growth Templates. *Nano letters.* **12**, 2784–2791 (2012).
12. Dave, M., Vaidya, R., Patel, S. G. & Jani, A. R. High pressure effect on MoS2 and MoSe2 single crystals grown by CVT method. *Bulletin of Materials Science.* **27**, 213–216 (2004).
13. Sim, H. *et al*. High-concentration dispersions of exfoliated MoS2 sheets stabilized by freeze-dried silk fibroin powder. *Nano Research.* **9**, 1709–1722 (2016).
14. Serres, J. M. *et al*. MoS2 saturable absorber for passive Q-switching of Yb and Tm microchip lasers. *Lasers & Electro-optics.* (2016).
15. Aiub, E. J., Steinberg, D., Ea, T. D. S. Ea & Lam, S. 200-fs mode-locked Erbium-doped fiber laser by using mechanically exfoliated MoS2 saturable absorber onto D-shaped optical fiber. *Optics Express.* **25**, 10546 (2017).
16. Kangpeng, W. *et al*. Ultrafast Saturable Absorption of Two-Dimensional MoS2 Nanosheets. *Acs Nano.* **7**, 9260 (2013).
17. Zhang, S. *et al*. Direct observationof degeneratetwo-photon absorption and its saturation, in ws2 and mos2 monolayer and few-layer films. *Acs Nano,* **9**, 7142 (2015).
18. Yang, H. *et al*. Giant two-photon absorption in bilayer graphene. *Nano Letters* **11**, 2622 (2011).
19. Shuxian, W. Broadband few-layer MoS2 saturable absorbers. *Advanced Materials.* **21** (2014).
20. Guan, X. *et al*. Self-Q-switched and wavelength-tunable tungsten disulfide-based passively Q-switched Er:Y_2O_3 ceramic lasers. *Photonics Research.* **6**, 830 (2018).
21. Luan, C. *et al*. WS2 as a saturable absorber for Q-switched 2 micron lasers, *Opt. Lett.* **41**, 3783–3786 (2016).
22. Zhang, M. *et al*. Yb- and Er-doped fiber laser Q-switched with an optically uniform, broadband WS2 saturable absorber. *Scientific Reports.* **5**, 17482–17482 (2015).
23. Duan, X. *et al*. Synthesis of WS2xSe2-2x Alloy Nanosheets with Composition-Tunable Electronic Properties. *Nano letters.* **16**, 264 (2016).
24. Tannous, J., Dassenoy, F., Bruhács, A. & Tremel, W. Synthesis and Tribological Performance of Novel Mo x W 1− x S 2 (0 ≤ x ≤1) Inorganic Fullerenes. *Tribology Letters.* **37**, 83–92 (2010).
25. Yu, P. *et al*. Metal–Semiconductor Phase-Transition in WSe2(1-x)Te2x Monolayer. *Advanced Materials.* **29** (2017).
26. Wang, Y. *et al*. Ultra-broadband Nonlinear Saturable Absorption for Two-dimensional Bi2TexSe3-x Nanosheets. *Scientific Reports.* **6**, 33070 (2016).
27. Lucarini, D. V., Peiponen, P. D. K.-E., Saarinen, D. J. J. & Vartiainen, D. E. M. Kramers-Kronig Relations in Optical Materials Research. *Springer.* **110** (2005).
28. Zhu, C. *et al*. A robust and tuneable mid-infrared optical switch enabled by bulk Dirac fermions. *Nature Communications.* **8**, 14111 (2017).
29. Khadka, S. *et al*. Ultrafast spectroscopy of exciton and exciton dynamics in mono and few layers of WS2. *Aps March Meeting.* (2016).
30. Glinka, Y. D., Babakiray, S., Holcomb, M. B. & Lederman, D. Effect of Mn doping on ultrafast carrier dynamics in thin films of the topological insulator Bi2Se3. *Journal of Physics Condensed Matter.* **28**, 165601 (2016).

Acknowledgements

Author contributions

Xinjie Lv, Gang Zhao, Zhenda Xie, Jinlong Xu and Shining Zhu conceived the original idea. Zhengting Du, Chi Zhang and Jinlong Xu designed and carried out the experiment. Zhengting Du and Chi Zhang contributed to the experimental characterization and interpretation. Zhengting Du and Mudong Wang contributed to the EDS measurement. Zhengting Du, Xuejin Zhang and Jian Ning contributed to the Raman spectrum measurement. Zhengting Du, Chi Zhang and Jinlong Xu produced the manuscript and interpreted the results. All authors participated in discussions and reviewed the manuscript.

Competing interests

The authors declare no competing interests.

Additional information

Correspondence and requests for materials should be addressed to Z.X. or J.X.

Reprints and permissions information is available at www.nature.com/reprints.

Publisher's note Springer Nature remains neutral with regard to jurisdictional claims in published maps and institutional affiliations.

9